INTERNATIONAL JOURNAL FOR NUMERICAL METHODS IN FLUIDS
Int. J. Numer. Meth. Fluids 2007; **53**:105–128
Published online 19 June 2006 in Wiley InterScience (www.interscience.wiley.com). DOI: 10.1002/fld.1251

Application of Chimera grid to modelling cell motion and aggregation in a narrow tube

B. Chung[1], P. C. Johnson[2] and A. S. Popel[1,*,†]

[1]*Department of Biomedical Engineering, School of Medicine, Johns Hopkins University, Baltimore, MD 21205, U.S.A.*
[2]*Department of Bioengineering, University of California, San Diego, La Jolla, CA 92093, U.S.A.*

SUMMARY

A computational scheme using the Chimera grid method is presented for simulation of three-dimensional motion and aggregation of two red blood cells (RBCs) in a narrow tube. The cells are modelled as rigid ellipsoidal particles; the computational scheme is applicable to deformable fluid-filled particles. Attractive energy between two RBCs is modelled by a depletion interaction theory and used for simulating aggregation of two cells. Through the simulation, we show that the Chimera grid method is applicable to the simulation of three-dimensional motion and aggregation of multiple RBCs in a microvessel and microvascular network. Copyright © 2006 John Wiley & Sons, Ltd.

Received 9 January 2006; Revised 7 April 2006; Accepted 11 April 2006

KEY WORDS: Chimera grid; red blood cell; RBC aggregation; depletion interaction energy

1. INTRODUCTION

Microvessels, particularly arterioles and venules, are the major site of blood flow regulation [1]. Blood in the microcirculation exhibits non-Newtonian behaviour. Since blood contains about 45% red blood cells (RBCs) by volume, as well as platelets and leucocytes, the interactions of these formed elements play a crucial role in determining blood characteristics. Because of their large volume fraction and their aggregation capacity, RBCs are the most important determinant of blood flow characteristics. The level of RBC aggregability is reported to increase in disease states such as diabetes mellitus, myocardial infarction and renal disease [2, 3]. Furthermore, aging

*Correspondence to: A. S. Popel, Department of Biomedical Engineering, School of Medicine, Johns Hopkins University, Baltimore, MD 21205, U.S.A.
†E-mail: apopel@jhu.edu

Contract/grant sponsor: NIH; contract/grant number: HL 52684

of RBCs affects the aggregation. For instance, the aggregability of old RBCs is reported to be 200% higher than that of young RBCs [3], and neonatal RBCs show reduced aggregation [4].

In vivo and *in vitro* studies of RBC aggregation have been conducted. Most *in vitro* experiments have been performed using a rotational viscometer [5, 6] and have shown an inverse relationship between the relative viscosity and shear rate at a low shear rate. *In vivo* experiments have also revealed such a relationship [7], even though *in vitro* studies using a vertical capillary tube showed viscosity to be independent of shear rate, as a result of the axial migration of RBCs and their aggregates and the formation of a cell-free or cell-depleted layer adjacent to the tube wall [8]. Because of the occurrence of frequent vascular junctions *in vivo*, a cell-free layer does not develop until the pseudo shear rate (mean velocity divided by diameter) falls below 5 s^{-1} [9]. Bishop *et al*. [10] have also reported bluntness of the velocity profile as a result of RBC aggregation at a low shear rate. Thus, velocity distribution in microvessels is shear-dependent, and the inverse relationship between RBC aggregation and shear rate causes the increase in vascular resistance. In order to elucidate the specific mechanisms responsible for diseases related to RBC aggregation, we need to better understand how RBC aggregation depends on vascular geometries, flow distribution and macromolecular composition of the blood plasma.

Two models of interaction energy have been proposed to account for RBC aggregation: bridging and depletion interaction. Chien and Jan proposed that macromolecules, such as fibrinogen, attach to the RBC surfaces (glycocalyx) and bridge them [11]; this theory is referred to as the bridging interaction model. The depletion interaction model for RBC aggregation has been introduced and formulated by Neu and Meiselman [12]. They proposed that as RBCs in a polymer solution approach each other, a depletion layer develops between the cells due to an imbalance between adsorption energy and the loss of entropy of the polymer and, as a result, the difference in osmotic pressure between the depletion zone and the bulk phase leads to displacement of the solvent into the bulk phase, minimizing the polymer-reduced space between cells. In the present study, we have used the depletion interaction model, as extended to describe interactions between non-planar surfaces.

The RBC is a biconcave disk of about 6–8 μm diameter and 2 μm thickness. It contains haemoglobin solution, with a viscosity about five times higher (6 cPs) than that of the surrounding plasma (1.2 cPs). The haemoglobin solution is enveloped by a flexible membrane, which is composed of a lipid bilayer and its associated proteins and an underlying cytoskeleton (spectrin, actin and other proteins). The proteins determine the structural integrity of the RBC. The deformability of the RBC has been studied by modelling the characteristics of the membrane based on continuum theory. A Neo-Hookean nonlinear model and Evans and Skalak model [13] have been used in previous studies [14, 15].

Various computational methods have been used to simulate the flow of discrete particles. These methods include the boundary integral method applied to the three-dimensional motion of a liquid capsule enclosed by a membrane [16], and the immersed boundary method (IB) combined with a finite element method (FEM) for the membrane to simulate large deformations of an RBC in a simple shear flow [14]. The IB method was also used to simulate RBC aggregation in a shear flow in two dimensions [17]. The IB method was further extended by an immersed FEM (IFEM) using a Lagrangian finite element solid mesh moving on top of an Eulerian finite element mesh, with higher accuracy enabling the fluid domain to have non-uniform meshes with arbitrary geometries and boundary conditions [18]. Other computational approaches that have been used to solve solid/fluid interaction problems are an extended FEM (X-FEM) using an analytic solution near a particle (enrichment scheme) [19] and a lattice Boltzmann method (LBM) originating

DOI: 10.1002/fld

from lattice gas (LG) automata. The LBM method was applied to describe leucocytes rolling in postcapillary expansions and the interactions with RBCs [20]. Subsequently, the LBM was applied to simulate RBC flows in microvessels to reproduce Fahraeus–Lindqvist and Fahraeus effects [21]; the calculations were two-dimensional, with RBCs represented as solid rectangles and leucocytes as solid circles.

In 1985, Dougherty developed a Chimera grid scheme [22], which has been generally applied to aerodynamic flows. This scheme uses separate fluid and particle grids for particle flows, and it is advantageous for simulations of flows in complex geometries. Generally, the Chimera grid method (i) provides easier mesh generation to build complex geometries, such as bifurcations for fluid domains and spheroidal particles for particle grids; (ii) prevents severe mesh distortion due to motions of particles in fluid domain that do not require mesh upgrade algorithms; and (iii) has capability to simulate the motions of flexible geometries via an arbitrary Lagrangian–Eulerian formulation (ALE) [23]. The method has been applied to describe the motion of a sphere at a low-to-intermediate range of $Re = 0.1$–100 [24] and the motion of an array of spheres [25].

In the present study, we have applied the Chimera grid scheme to simulate the motion and aggregation of RBCs in a cylindrical tube, based on the depletion interaction model [12]. RBCs are modelled as solid ellipsoidal particles with eccentricity ratio $e = 0.5$ (oblate spheroid), and a steady Poiseuille flow condition is assumed at the inlet of the tube. Since ellipsoidal particles have not been simulated in a low Re regime using this method, and Chimera method has not been applied to the simulation of RBC aggregation previously, our objectives in this study are (i) to construct an algorithm to simulate the flow of particles at a low Re using the Chimera grid method, (ii) to apply the method to simulate the motion of two solid particles in a straight narrow tube without and with aggregation based on the depletion interaction model, and (iii) to demonstrate its feasibility for computing the motion of multiple ellipsoidal particles. The method has the potential to be further extended to deformable particles with properties similar to RBCs.

Mathematical and numerical models based on Chimera grid method are presented in Sections 2.1–2.5. We validate the Chimera grid method by solving flow past a quiescent particle with both uniform and parabolic flows in Section 2.6 and comparing the results to known experimental data and theoretical solutions. Results for two RBCs with and without aggregation in a narrow tube are presented in Section 3.

2. METHODS

2.1. Chimera grid generation and interpolation between grids

We consider two computational domains to solve the flow past a spherical or ellipsoidal particle in a straight cylindrical tube. The computational domains represent the flow in the tube and the flow near the particle (Figure 1). We define the cylindrical domain to be the ‘major grid’ representing the fluid in the tube and spherical or ellipsoidal domain, and the ‘minor grid’, placed over the major grid, representing the fluid near the particle. The minor grid includes the sphere or ellipsoid. These two independent grids can communicate through nonconservative trilinear interpolation at the boundary of each grid. The figure also shows ‘fringe points’ (solid circles) that surround the particle in the major grid. Fringe points of the minor grid are marked as open circles. Pressure and velocity are interpolated at these fringe points. The governing equations described below are not solved at the points of the major grid that fall inside the particle in the present study; the method is expandable to deformable particles, in which case the internal points will be used.

DOI: 10.1002/fld

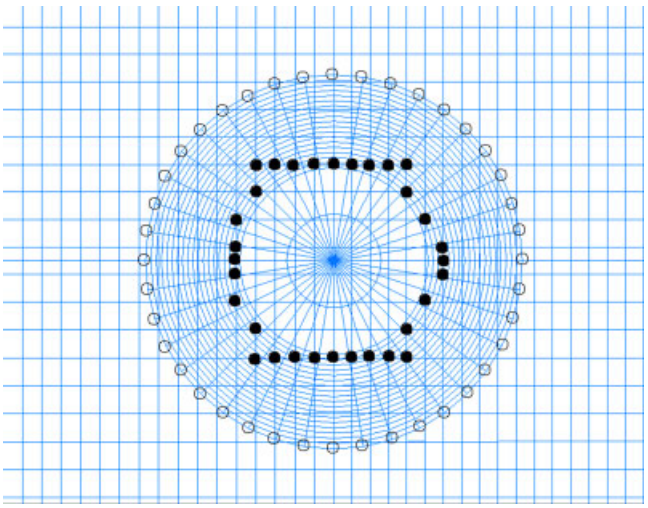

Figure 1. Fringe points of major and minor grids.

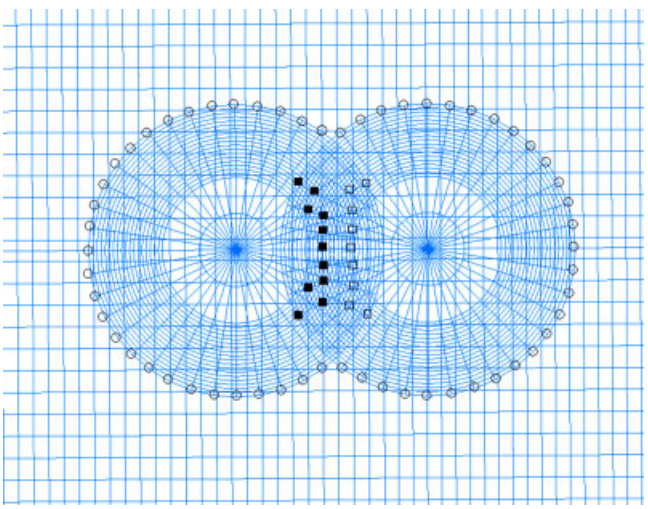

Figure 2. Fringe points of major and minor grids when two particles are close together.

When two or more particles are immersed in the fluid, fringe points between minor grids that represent the two particles must also be considered. Figure 2 shows the fringe points when two particles are close to each other. The fringe points of two minor grids marked by open circles are the points of interpolation between major and minor grids. Interpolation between the two minor grids is performed through the fringe points marked by open and solid squares (open for the left particle, solid for the right particle). The points of each particle completely envelop the surface of

DOI: 10.1002/fld

the other particle. The fringe points of the major grid are the points that surround the particles. Further details of the grid generation and interpolation method are presented in Appendix A.

2.2. Governing equations

Blood as a suspension exhibits non-Newtonian behaviour at low shear rates, primarily due to RBC aggregation. However, the blood plasma is a Newtonian fluid, thus the equations governing the flow around RBCs can be written in the integral form as

$$\int \mathbf{v} \cdot \mathbf{n} \, \mathrm{d}A = 0 \tag{1}$$

$$\int \rho \frac{\partial \mathbf{v}}{\partial t} \, \mathrm{d}V + \int \rho(\mathbf{v} \cdot \nabla)\mathbf{v} \, \mathrm{d}V = -\int p\mathbf{n} \, \mathrm{d}A + \int \boldsymbol{\tau} \cdot \mathbf{n} \, \mathrm{d}A \tag{2}$$

where $\mathbf{v}$, p, ρ, and $\boldsymbol{\tau}$ are the velocity, pressure, density of the fluid and stress tensor, respectively. The stress tensor is given by

$$\boldsymbol{\tau} = \mu(\nabla \mathbf{v} + \nabla \mathbf{v}^{\mathrm{T}}) \tag{3}$$

where μ is the viscosity of the fluid.

RBCs experience a drag force due to the flow and an interaction force between the two cells when they are close to each other. By ignoring body force, the equation of motion for the particle is

$$m \frac{\mathrm{d}\mathbf{v}_{\mathrm{c}}}{\mathrm{d}t} = \mathbf{F}^{\mathrm{D}} + \mathbf{F}^{\mathrm{A}} \tag{4}$$

where m and $\mathbf{v}_{\mathrm{c}}$ are the mass and translational velocity of the RBC, respectively, the drag force $\mathbf{F}^{\mathrm{D}}$ exerted by the fluid on the particle is in the form

$$\mathbf{F}^{\mathrm{D}} = -\int p\mathbf{n} \, \mathrm{d}A + \int \boldsymbol{\tau} \cdot \mathbf{n} \, \mathrm{d}A \tag{5}$$

and $\mathbf{F}^{\mathrm{A}}$ is the interaction force based on the depletion interaction model [12]. The moment of momentum equation for the particle is

$$I \frac{\mathrm{d}\boldsymbol{\omega}}{\mathrm{d}t} + \boldsymbol{\omega} \times I \cdot \boldsymbol{\omega} = \mathbf{T}^{\mathrm{D}} + \mathbf{T}^{\mathrm{A}} \tag{6}$$

where I and $\boldsymbol{\omega}$ are the moment of inertia and angular velocity of the cell, respectively, and $\mathbf{T}^{\mathrm{A}}$ is the torque due to the interaction force $\mathbf{F}^{\mathrm{A}}$, and the torque $\mathbf{T}^{\mathrm{D}}$ exerted by the fluid on the particle is in the form

$$\mathbf{T}^{\mathrm{D}} = -\int \mathbf{r}_{\mathrm{c}} \times p\mathbf{n} \, \mathrm{d}A + \int \mathbf{r}_{\mathrm{c}} \times \boldsymbol{\tau} \cdot \mathbf{n} \, \mathrm{d}A \tag{7}$$

where $\mathbf{r}_{\mathrm{c}}$ is the position vector from the centre of mass and the surface of the cell. Appendix B describes the depletion interaction model of Neu and Meiselman [12] and its application to particles of arbitrary shape [26]; the derivations of the interaction force $\mathbf{F}^{\mathrm{A}}$ and torque $\mathbf{T}^{\mathrm{A}}$ based on the depletion interaction model are also described.

DOI: 10.1002/fld

2.3. Boundary conditions

For the simulation of motion of two RBCs with and without aggregation in a narrow tube, no-slip conditions at the tube wall, Γ_w, and a fully developed flow condition at the inlet, Γ_i, are specified

$$\mathbf{v}|_{\Gamma_w} = 0 \tag{8}$$

$$\mathbf{v}|_{\Gamma_i} = v_{max}\left(1 - \frac{r^2}{R^2}\right) \tag{9}$$

where v_{max}, r and R represent the maximum fluid velocity at the inlet, radial position and radius of the tube, respectively. At the outlet of tube, Γ_o, we specify the zero axial velocity gradient

$$\left.\frac{\partial \mathbf{v}}{\partial z}\right|_{\Gamma_o} = 0 \tag{10}$$

where z is the axial position in the tube.

The boundary condition at the surface of the RBC, Γ_c, is specified using the cell's translational and rotational velocities

$$\mathbf{v}|_{\Gamma_c} = (\mathbf{v}_c + \boldsymbol{\omega} \times \mathbf{r}_c)|_{\Gamma_c} \tag{11}$$

2.4. Numerical methods

The governing equations are discretized based on the body-fitted coordinates explained in Appendix A and solved by Chorin's pressure correction method [27]. Details of the solution method are described in Appendix C. The translational and angular velocities of each cell are determined by the resultant force and torque in Equations (B17) and (B18) through Newton's law in Equations (4) and (6). Numerically, we discretize these two equations based on the implicit scheme. However, because of the very small inertia of RBCs at a low Re, excessive computational time is required to simulate particle motion because a very small time step is required to obtain the acceleration of the particle. Hence, we formulated an algorithm to compute a small force and torque on a particle using a larger time step. We discretize Equation (4) based on the implicit method with intermediate time. The current particle translational velocities are obtained by

$$\mathbf{v}_c^{n+1,m+1} = \mathbf{v}_c^{n+1,m} + \frac{\Delta t'}{m}\frac{\mathbf{F}(\mathbf{v}^{n+1,m+1}, p^{n+1,m+1}) + \mathbf{F}(\mathbf{v}^n, p^n)}{2} \tag{12}$$

where the superscripts n and $n+1$ stand for old and new time, m and $m+1$ stand for the previous and current iterations, respectively, and $\Delta t'$ is a time step whose value can be arbitrarily chosen. Therefore, the translational velocities at the current iteration, $m+1$, are updated using velocities obtained at the previous iteration, m, and the average value of the forces obtained at the old time, n, and the current $m+1$ iteration. The value of $\Delta t'$ can be chosen to be small enough to yield correct velocities at the current iteration, $m+1$. Likewise, Equation (6) is solved by a fourth-order Runge–Kutta method to obtain the current $\boldsymbol{\omega}^{m+1}$ using the previous $\boldsymbol{\omega}^m$, $\Delta t'$ and the average value of torques obtained at the old time, n, and the current $m+1$ iteration. This algorithm calculates the particle acceleration at each iteration and then yields a particle velocity within the actual time step Δt, ultimately resulting in a zero resultant force and torque at a given time. Employing this algorithm allows us to obtain the motion of a particle for a reasonable time interval by using a larger time step.

DOI: 10.1002/fld

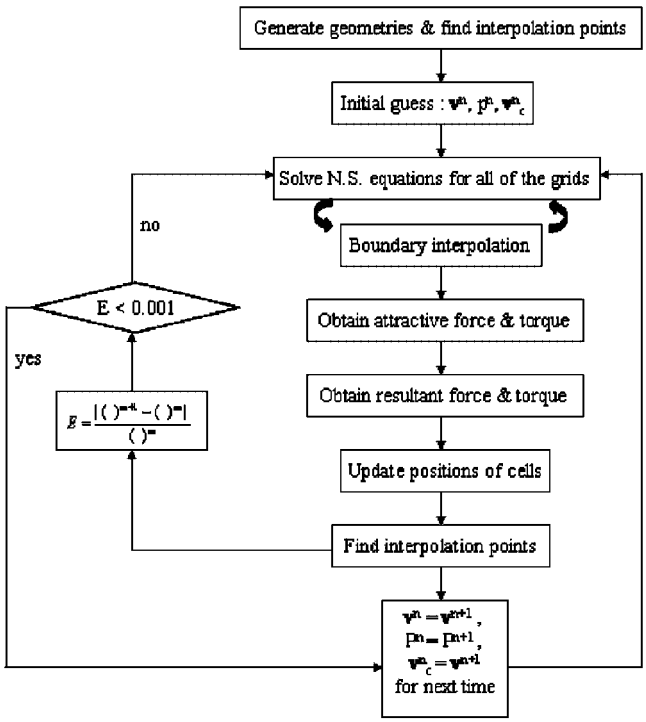

Figure 3. Flowchart of overall iterative steps for numerical solution.

Navier–Stokes equations and equations for the motion of cells, with all the algorithms, including the depletion interaction between cells as described in Appendices B and C, are solved based on the following overall iterative steps, as illustrated in the flowchart in Figure 3:

(1) Generate geometries and identify fringe points and holes in each grid for interpolation.
(2) Guess the old velocity $\mathbf{v}^n$, pressure p^n and cell velocity $\mathbf{v}^n_c$.
(3) Solve Navier–Stokes equations using the following steps:
   (i) Solve the vortical velocity $\mathbf{v}'$ using Equation (C3).
   (ii) Solve Equation (C5) to obtain the velocity potential ϕ using the vortical velocity and the Poisson equation Equation (C6) to obtain the irrotational velocity $\mathbf{v}_o$.
   (iii) Solve Equation (C4).
   (iv) Make velocity and pressure corrections using Equations (C1) and (C2).
(4) Interpolate the solution to fringe points of other grids, and repeat steps 3–4 for all of the grids.
(5) Find intercellular distances between the surface elements of the cells, and evaluate the attractive force and torque using the distances as described in Appendix B and drag force and torque due to the flow.
(6) Using the resultant force and torque on cells, determine the positions of the cells.
(7) Identify the holes and fringe points of all the major and minor grids.

DOI: 10.1002/fld

(8) Evaluate the error norm of the velocity and pressure for each grid, which is defined by

$$E = \frac{|()^{m+1} - ()^{m}|}{()^{m}} \tag{13}$$

where $()^{m+1}$ and $()^{m}$ are the velocity or pressure at the current and previous iterations, respectively.

(9) Repeat steps 3–8 until the maximum norm $E_{\max}$ over the entire grid is less than 0.001.

(10) The velocity, pressure for all of the grid points and cell velocity obtained by the above steps are used as the old velocity $\mathbf{v}^n$, pressure p^n and cell velocity $\mathbf{v}_c$ and go back to step 3 and repeat steps 3–9 for next time.

All simulations were carried out on a 3.20 GHz Pentium 4 PC; a typical simulation with two cells takes approximately 30 h.

2.5. Assumption for the elimination of particle overlap

Numerically, it is possible that two solid domains (Figure 2) representing particles may overlap as the two particles approach each other. In order to prevent the overlap, we use an electrostatic repulsive energy described in Equations (B5) and (B6) to simulate the motions of two RBCs. As shown in Figure 10(a), the interaction energy gradually becomes zero and changes its sign as a result of the repulsive energy when the intercellular distance h between RBCs approaches approximately twice the thickness of the RBC glycocalyx, depending on the type of polymer present in the plasma and on the polymer concentration. Therefore, when the minimum intercellular distance $h_{\min}$ between the surfaces of the two particles with arbitrary shapes is within the range in which the electrostatic energy dominates, the two particles repel each other, preventing the overlap. We apply the electrostatic energy to the simulations with and without aggregation to avoid the overlap of two RBCs.

2.6. Validation problems

As the first step in solving problems involving particulate flows, we simulate flows past a fixed particle in unbounded and bounded fluid domains. For this purpose, we considered three validation problems, as follows:

(1) Flow past a quiescent sphere immersed in an unbounded domain with uniform inlet flow.
(2) Flow past a quiescent sphere located in a straight tube with a parabolic inlet flow.
(3) Flow past a quiescent ellipsoid located in a straight tube with a parabolic inlet flow.

Several authors have reported empirical relationships between the drag coefficient C_D and Re for the first problem. Flow past a sphere immersed in a straight tube has been solved analytically by a reflection method [28]. Wakiya reported the analytic solution for a spheroid immersed in a Poiseuille flow through a tube [29]. Prior to the validation problems, a mesh refinement study was performed using the second problem at $Re = 0.1$. Several empirical relationships between C_D and Re were compared to the numerical results of the first validation problem. The comparison was made according to the range of Re. For $Re > 1$, three empirical relationships were considered, as follows:

$$C_D = \frac{24}{Re}(1 + 0.197Re^{0.63} + 0.00026Re^{1.38}) \quad \text{for } 1 < Re < 100 \tag{14}$$

DOI: 10.1002/fld

$$C_D = \frac{24}{Re}(1 + 0.125Re^{0.72}) \quad \text{for } Re < 1000 \tag{15}$$

$$C_D = \frac{24}{Re}(1 + 0.15Re^{0.687}) \quad \text{for } Re < 800 \tag{16}$$

These relationships were reported by Langmuir and Blodgett (Equation (14)), Lapple (Equation (15)) and Schiller and Nauman (Equation (16)), respectively [30]. For $Re < 1$, the following empirical relationships were considered:

$$C_D = \frac{24}{Re}(1 + 0.1315Re^{0.82-0.05\log(Re)}) \quad \text{for } 0.01 < Re < 20 \tag{17}$$

$$C_D = 0.28 + \frac{6}{Re^{0.5}} + \frac{21}{Re} \quad \text{for } 0.1 < Re < 4000 \tag{18}$$

$$C_D = 0.48 + 28Re^{-0.85} \quad \text{for } 0.2 < Re < 2000 \tag{19}$$

$$C_D = \frac{24}{Re} \quad \text{for } Re = 0 \tag{20}$$

reported by Beard (Equation (17)), Kurten *et al*. (Equation (18)), Gilbert *et al*. (Equation (19)) and Stokes law (Equation (20)) [30].

2.6.1. Mesh refinement study. Mesh refinement study was performed at a fixed $Re = 0.1$ to obtain appropriate mesh densities for the problem of cell motion in the tube flow. The major grid represents a tube with a diameter larger than the cell diameter (ratio of D_{cell} to $D_{tube} = 0.25$), which represents a finite domain for this study, and the minor grid represents a sphere. A no-slip boundary condition is applied at the tube wall Γ_w. I, J, K indices stand for the total mesh densities in the ξ, η, ζ directions. The mesh was refined by increasing the values of I, J, K so that nine cases were considered. The mesh was then further refined in the region near the sphere, as shown in Figure 4. Table I shows the values of I, J, K for both the major and minor grids for nine different

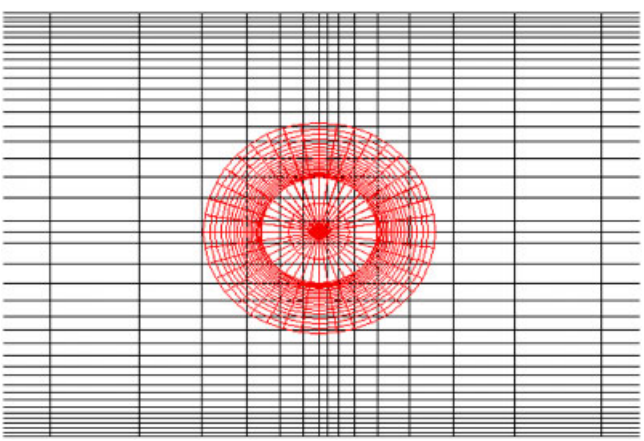

Figure 4. Mesh densities of major and minor grids.

DOI: 10.1002/fld

Table I. Mesh densities of major and minor grids.

Case	1 Major Minor	2 Major Minor	3 Major Minor	4 Major Minor	5 Major Minor	6 Major Minor	7 Major Minor	8 Major Minor	9 Major Minor
I	12	15	16	17	18	19	20	21	22
	12	15	16	17	18	19	20	21	22
J	12	15	16	17	18	19	20	21	22
	12	15	16	17	18	19	20	21	22
K	17	17	18	18	18	20	20	21	22
	12	15	16	17	18	19	20	21	22

Table II. Drag forces obtained in mesh refinement study.

Case	1	2	3	4	5	6	7	8	9
F^{D}	0.952	0.910	0.865	0.866	0.872	0.900	0.924	0.92	0.917

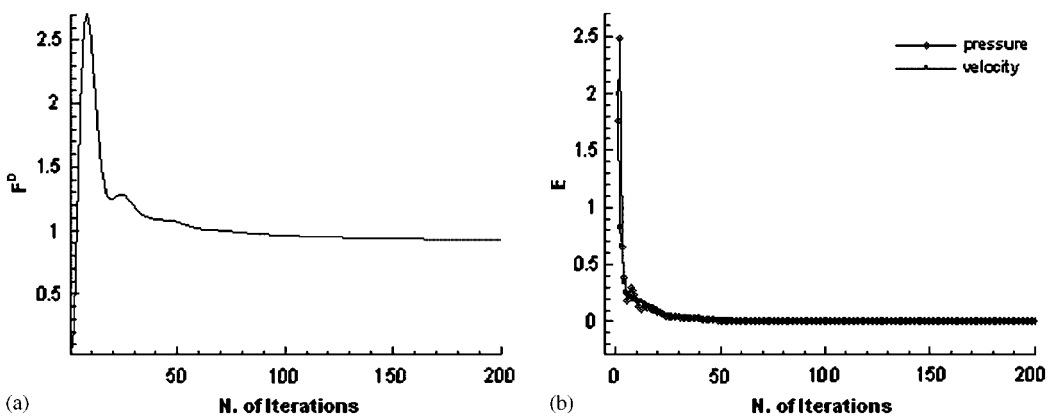

Figure 5. (a) A representative figure of the convergence of the drag force for $Re = 0.1$; and (b) a convergence curve of the error norm E of pressure and velocity for $Re = 0.1$.

cases. Case 1 is the coarsest, and Case 9 is the finest mesh case. As seen in Table II, the rate of change in drag force, F^{D}, between Cases 8 and 9 was within 0.5% so that Case 8 could be used for the rest of computations in this study. Shown in Figure 5(a) is the representative convergence of drag force, F^{D}, for Case 8. Figure 5(b) represents a convergence curve of the error norm of pressure and velocity defined in Equation (13) for the same case.

2.6.2. Example 1. Flow past a sphere in an unbounded domain was solved for $Re = 0.5$, 1, 10, 30 and 50. Uniform velocity was specified at the inlet. The boundary conditions, Equations (8) and (10), were used with zero velocity of the sphere in Equation (11). Based on the mesh density

DOI: 10.1002/fld

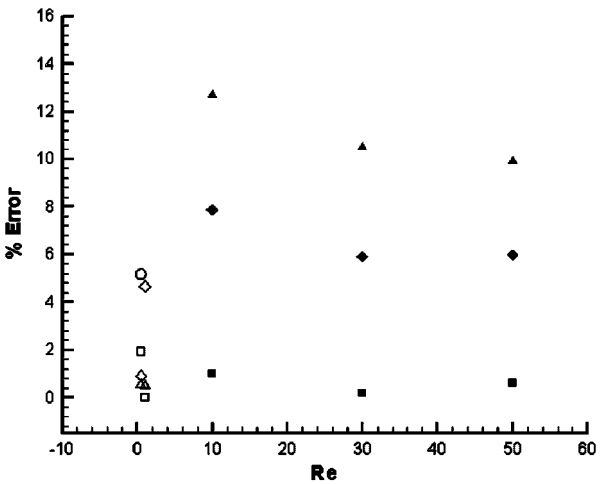

Figure 6. Percent error for the comparison of computed C_D and empirical C_D for a sphere in an unbounded domain; the open square, triangle, diamond and circle represent comparisons with Beard (Equation (17)), Kurten *et al.* (Equation (18)), Gilbert *et al.* (Equation (19)) and Stokes law (Equation (20)), respectively. The solid square, triangle and diamond represent comparisons with Langmuir and Blodgett (Equation (14)), Lapple and Schiller (Equation (15)) and Nauman (Equation (16)), respectively.

case, Case 8, we compared the computed C_D to the empirical C_D according to the range of Re. Percent error, which is defined by

$$\% \text{ error} = 100 \frac{C_D^{\text{computed}} - C_D^{\text{empirical}}}{C_D^{\text{empirical}}} \tag{21}$$

were evaluated for all of the Re considered (Figure 6). The lowest errors for all of the Re considered were within 1%. Note that in all cases the computed C_D is larger than the empirical value, most likely reflecting the effect of the finite domain size, since the domain diameter is only four times the particle diameter.

2.6.3. Example 2. Flow past a quiescent sphere placed in a straight cylindrical tube was solved at $Re = 0.1$. First, the sphere was located at the centreline of the tube. Second, the sphere was located away from the centreline of the tube at $b/R = 0.3$, where R is the radius of cylinder and b is the distance from the centreline. Parabolic flow, Equation (9), was specified at the inlet Γ_i of the tube. Other boundary conditions were Equations (8) and (10) with zero velocity of the sphere. Happel and Brenner [28] have reported analytic solutions for drag force and torque acting on a sphere in a fluid flow using the reflection method. The calculated drag force and torque acting on the surface of the sphere in the tube were compared with the analytic solutions.

The solutions using the reflection method are $F^D = 0.876$ and $T = 0.01525$ at $Re = 0.1$ in the second case. From our simulation, the drag force and torque calculated were $F^D = 0.8763$ and $T = 0.01567$, so that the discrepancies between them were within 2.7% for both the drag force and torque. In the first case when the sphere is at the centre, $b = 0$, the value of F^D based on

DOI: 10.1002/fld

Haberman's exact theory [28] is 0.91 at $Re = 0.1$, and our calculated drag force F^D was 0.92, so that the discrepancy between them was less than 1%.

2.6.4. Example 3. Flow past an ellipsoid with an eccentricity ratio $e = 0.5$ (prolate spheroid) placed in a straight tube was simulated at $Re = 0.1$. The ellipsoid was placed at the centreline of the tube, its longest axis coinciding with the tube axis. The ratio of the longest semiaxes of the ellipsoid to the tube radius was 0.25. Parabolic flow, Equation (9), was imposed at the inlet of the tube. Equations (8) and (10) with zero velocity of the ellipsoid were specified at the other boundaries of the tube. Drag force acting on the ellipsoid immersed in a Poiseuille flow through the pipe at $Re = 0.1$ was 0.404, based on the analytic solution in Reference [29]. Our computation showed that drag force was 0.417, so that the discrepancy was 3%.

3. RESULTS FOR TWO CELLS

In this study, we modelled the shape of the RBC as a solid ellipsoidal particle. The eccentricity of the ellipsoid was fixed at 0.5 in all our simulations. The density of the cell was the same as that of plasma. The motion of two cells in Poiseuille flow in a tube was simulated. The first computation was performed for the case in which the aggregability of the RBCs was negligible, so that the attractive force between two cells is not considered. The second simulation was the motion of two cells forming an aggregate. The governing equations with the boundary conditions discussed in the earlier sections were solved at a fixed $Re = 0.1$.

Note that for a microvessel with 20 μm diameter, the average plasma velocity is 0.5 cm/s at $Re = 0.1$. The dimensions for the model are similar to those found in postcapillary venules where aggregates first form *in vivo* [31]. From our dimensional analysis based on the vessel dimension and plasma properties, the relationship between the computed and actual values (MKS units) are found by

$$\begin{aligned} t_{act} &= 10^{-4} t_{com}, \quad v_{act} = 10^{-1} v_{com}, \quad L_{act} = 10^{-5} L_{com} \\ p_{act} &= 10 p_{com}, \quad F_{act} = 10^{-9} F_{com} \end{aligned} \tag{22}$$

where $()_{act}$ and $()_{com}$ are the actual and computed values, respectively. L represents the length.

3.1. Non-aggregating cells

Three cases were considered for different initial positions of two cells. In the first case, two cells were located symmetrically in the upstream region of the tube (Figure 7(a)). As time elapses, the two cells move downstream in the tube due to the flow, with a slight rotation because of the difference in velocity between the sides of the ellipsoid, as shown in the figure. The next case was the computation of the motion of one cell A, which was initially located at the centreline of upstream of the tube, and cell B, whose initial position was off the centreline of the tube at $b/R = 0.3$ downstream from cell A. Figure 7(b) shows the trajectories of the two cells. Cell A moves faster than cell B because of the parabolic velocity profile of the fluid. Furthermore, cell B rotates with the flow and cell A does not rotate much. Because of the differences in the cell velocities, cell A catches up with cell B as time progresses. Note that the velocity of a particle is always less than the fluid velocity at the location of the centre of mass of the particle. For the third

DOI: 10.1002/fld

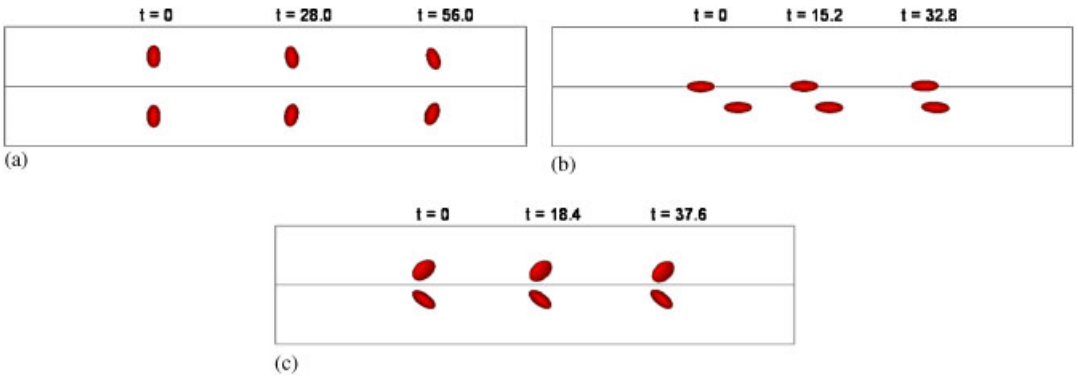

Figure 7. Trajectories of non-aggregating cells: (a) Case 1; (b) Case 2; and (c) Case 3.

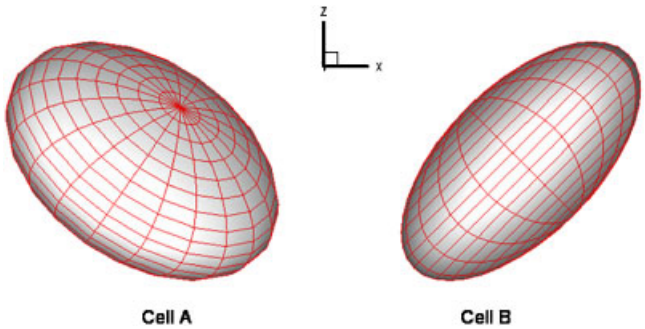

Figure 8. Initial positions of the two cells in Case 3.

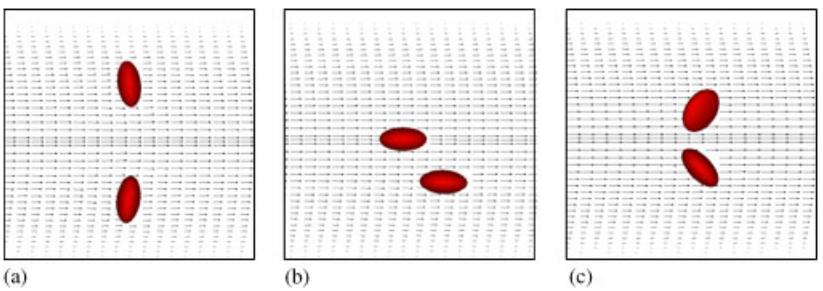

Figure 9. Velocity profiles for non-aggregating cells: (a) Case 1 at $t = 28.0$; (b) Case 2 at $t = 15.2$; and (c) Case 3 at $t = 18.4$.

simulation, two cells were located symmetrically upstream, but one cell, A, was tilted 45° with respect to the y and z axes of a rectangular coordinate system, and the other cell, B, was tilted 45° with respect to the y-axis only as shown in Figure 8. Since the two particles were initially

DOI: 10.1002/fld

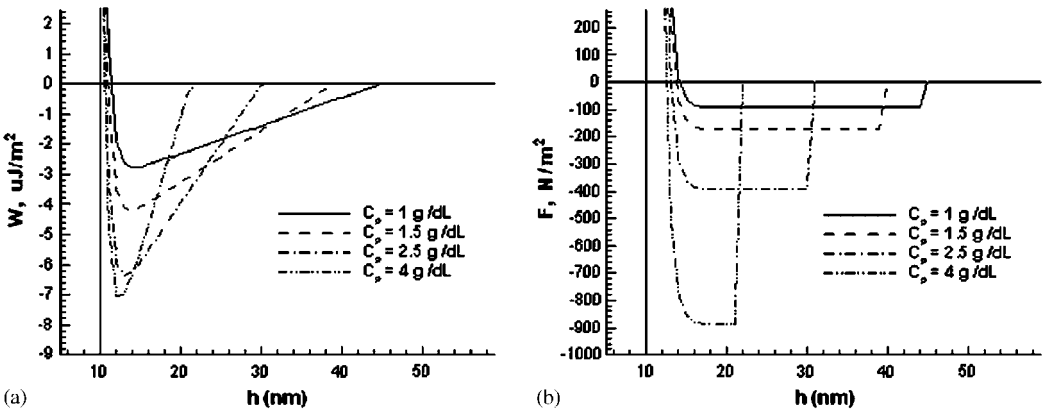

Figure 10. (a) Interaction energy vs. intercellular distance for DEX 500; and (b) interaction force vs. intercellular distance for DEX 500.

positioned near the centreline, where shear force is almost negligible, the cells move downstream without noticeable rotation (Figure 7(c)). Figure 9 shows the velocity profiles at different times for the three cases.

3.2. Aggregating cells

Based on the interaction energy, which accounts for both the depletion and electrostatic energies described in Appendix B, the attractive force depending on the type of polymer and its concentration, C_p, Equation (B13) was obtained. Figure 10(a) represents the interaction energies for Dextran 500 with $C_p = 1$, 1.5, 2.5 and 4 g/dl with respect to intercellular distance, h. In this case the penetration constant, C_b, was fixed at 1 g/dl. As the concentration C_p increases, the interaction energy increases, and the size of the region in which interaction occurs decreases. The attractive forces corresponding to the energy curves shown in Figure 10(a) are plotted in Figure 10(b). As expected, the force is reduced as C_p decreases. However unlike the energy curves, the attractive forces do not vary significantly across the region in which the interaction energies are effective; this is because the force is a derivative of energy with respect to distance, and the energy tail is a linear function of distance according to Reference [12].

Figure 10(a) shows that cell–cell interactions due to the depletion energy occur at the separation distances in the range of approximately 12–30 nm. However, our grid size, even near the cell, was significantly larger ($\sim$1 μm). This grid size can be reduced if necessary and is, theoretically, limited only by the computer hardware used; however, there is a practical limit to how far the grid size can be reduced. For this reason, the size of the region in which the attractive energy is effective is scaled up, keeping the value of the force the same. In this study, the scaling factor was fixed at 50 such that the glycocalyx thickness of the RBC was considered to be about one-tenth the height of the cell (0.25 μm). Therefore, the intercellular distance for our computations was about 50 times larger than the actual intercellular distance (Figure 11).

Three cases for the trajectories of two RBCs undergoing aggregation in a narrow straight tube were investigated, reflecting different initial positions of the RBCs. The polymer, Dextran 500 was used at a concentration, $C_p = 1.5$ g/dl. The levels of Dextran 500 used are relevant to

DOI: 10.1002/fld

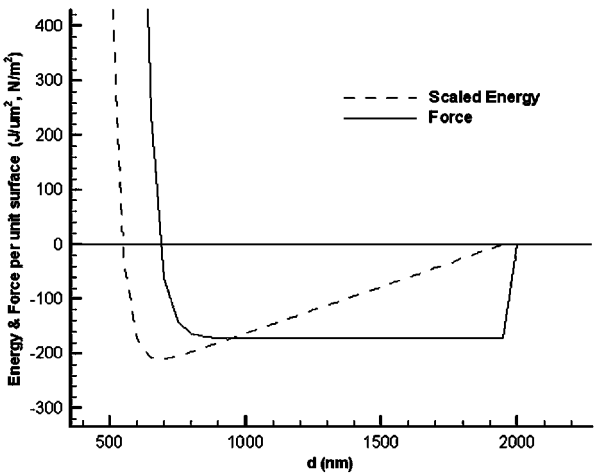

Figure 11. Interaction energy scaled up by a scaling factor of 50.

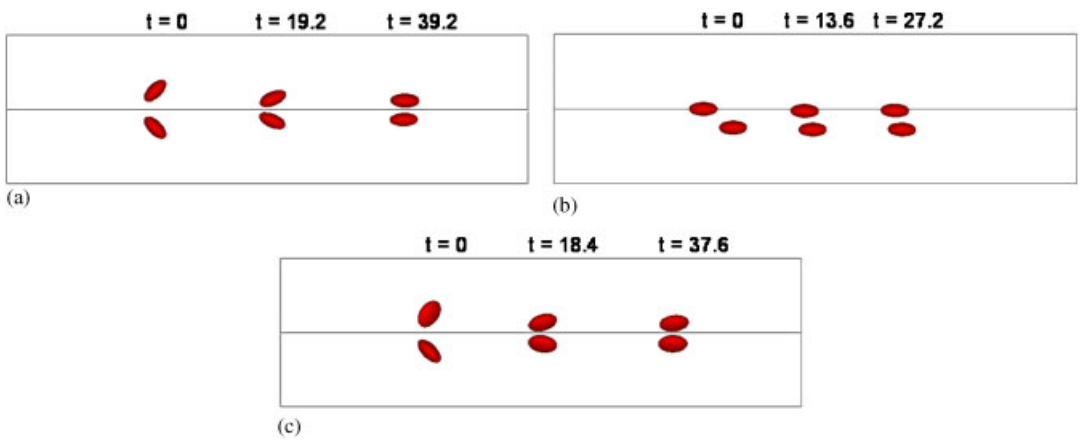

Figure 12. Trajectories of aggregating cells: (a) Case 1; (b) Case 2; and (c) Case 3.

in vivo studies. Bishop *et al.* [10, 32] and Kim *et al.* [31] used concentration of 0.6 g/dl, which produces a level of aggregability similar to that seen in normal humans, while Durussel *et al.* [33] and Mchedlishvili *et al.* [34] used concentrations of 4.1 and 4.8 g/dl which would elevate aggregability to a level equal to or greater than that seen in human disease states. The computation was performed for two cells that were initially positioned in the upstream region of the tube. The first case was simulated for the two cells initially tilted 45° with respect to the y-axis and facing each other at the centreline of the tube (Figure 12(a)). Because of attractive depletion forces, the two cells approach each other, moving downstream with time as shown in the figure. The cells initially rotate in the direction of the attractive force. When the cells approach more closely, repulsive forces come into effect.

DOI: 10.1002/fld

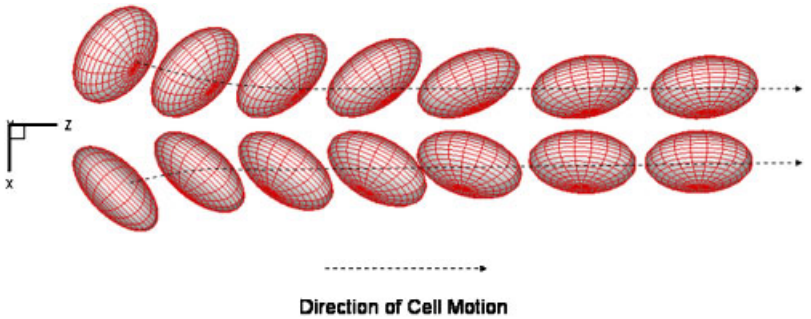

Figure 13. Cell trajectory in Case 3.

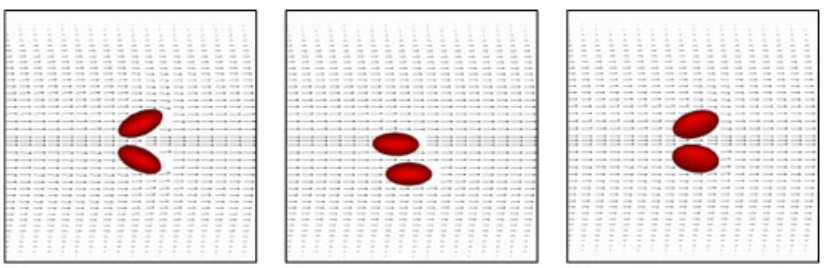

Figure 14. Velocity profiles for aggregating cells: (a) Case 1 at $t = 19.2$; (b) Case 2 at $t = 13.6$; and (c) Case 3 at $t = 18.4$.

As a second case, we computed the motion of one cell A, which was initially positioned at the centreline in the upstream region of the tube, and cell B, which was off the centreline at $b/R = 0.25$, downstream from cell A (Figure 12(b)). As in the case of the non-aggregating cells, cell A moves faster than cell B and catches up with cell B. However, unlike the case for non-aggregating cells, the aggregating force between the cells increases the speed of cell A and decreases the speed of cell B. As a result, cell A catches up with cell B faster than in the case of non-aggregating cells and moves toward cell B, moving slightly off the centreline of the tube.

A third case considered the same initial positioning of two cells as in the third case for non-aggregating cells (Figure 8). As we observed for the first case, the cells approach each other because of the attractive force and move downstream in an equilibrium position (Figure 12(c)). Figure 13 shows that due to attractive and repulsive forces cells A and B rotate with respect to both the y and z axes, finally attaining an equilibrium position with their flat surfaces facing each other. Velocity profiles for aggregating cells at several times are shown in Figure 14.

4. SUMMARY AND DISCUSSION

Because of the physiological and clinical significance of RBC aggregation in the microcirculation, there is a need for detailed numerical studies of RBC aggregation at the cellular level, as a mean of elucidating the relevant biophysical mechanisms in physiological and pathological states. In this

DOI: 10.1002/fld

study, we have used a Chimera grid method to investigate the 3-D motion and aggregation of two RBCs modelled as rigid ellipsoidal particles in a straight narrow tube. The method was validated for fully developed flow past a sphere and an ellipsoid in a tube. The aggregation force between RBCs was derived based on the depletion interaction model [12], extended to cells of arbitrary shape using the surface element integration [26].

The algorithm proposed in Section 2.4 is able to simulate the motion of a particle at low Re using a realistically large time step. Using the algorithm, we have described the motion of two ellipsoidal particles representing RBCs immersed in a Poiseuille flow in a straight narrow tube. The other novelty of this study is that the aggregation of two particles was simulated based on the depletion interaction model.

The computational limitation in dealing with the actual range in which the interaction energy between the cells acts depends on the grid size. Using the grid sizes we employed, we scaled up the depletion interaction distances by a factor of 50, retaining the magnitude of the force. As a result, the two cells never approaches closer than a distance of $h_{\min} = 500$ nm. The scaling factor was chosen so that the computational minimum intercellular distance $h_{\min}$ can be at least greater than the step size of the major grid within the region between two cells. Introducing the finer mesh of the major grid within the region between two cells could give us a computational intercellular distance that more closely approaches the physical intercellular distance.

The Chimera grid method allows us to deal with more complex geometries than merely a straight tube, including bifurcating vessels and more than two particles, by adding more minor grids representing RBCs. These modifications should enable us to compute the motion and aggregation of multiple RBCs in arterioles and venules. In the present study, the RBC is modelled as a rigid ellipsoidal particle. However, the RBC is in fact deformable, and its membrane properties can be described by the Neo-Hookean nonlinear model or the Evans and Skalak model. The method introduced in this study can be extended to describe the motion and aggregation of multiple deformable RBCs using an approach involving the arbitrary Lagrangian–Eulerian method (ALE), introduced by Hu [23].

APPENDIX A: GRID GENERATION AND INTERPOLATION METHOD

In order to construct three-dimensional computational domains, a generalized coordinate system (ξ, η, ζ) for the body-fitted grids is introduced based on Cartesian coordinates (x, y, z). As will be discussed later, the governing equations are discretized based on the generalized coordinates through the coordinate transformation. The generation of grids that represent a sphere or an ellipsoid in a straight tube is made using various types of control volumes, which include four-, five- and six-sided cells (Figure A1). A tube is composed of five-sided cells at the centreline and six-sided cells elsewhere (see also Figure A1). A sphere or ellipsoid is constructed with four- and five-sided cells at the centre point and six-sided cells elsewhere.

The communication between grids is achieved by trilinear interpolation at the fringe points. Searching the fringe points is accomplished by dividing the cell, which contains fringe points, into a number of tetrahedra. Therefore, a fringe point may fall into a tetrahedron of the cell, as shown in Figure A2. The known variables, $g_i(x_i, y_i, z_i)$ $(i = 1, 2, 3, 4)$, at the four vertices of the tetrahedron are used for interpolation (see also Figure A2). The unknown variable $g(x', y', z')$ for the given fringe point coordinates are then found by

$$g(x', y', z') = a_1 + a_2 x' + a_3 y' + a_4 z' \tag{A1}$$

DOI: 10.1002/fld

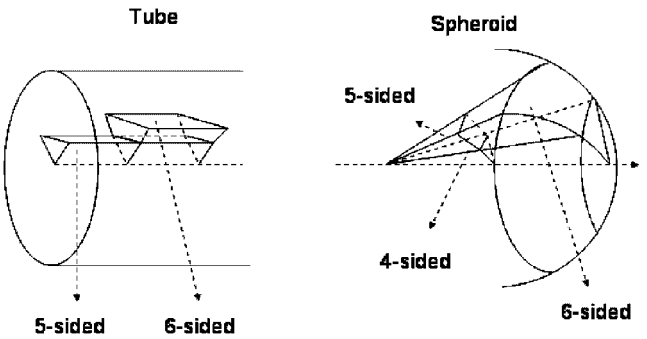

Figure A1. Computational elements for a tube and a spheroid.

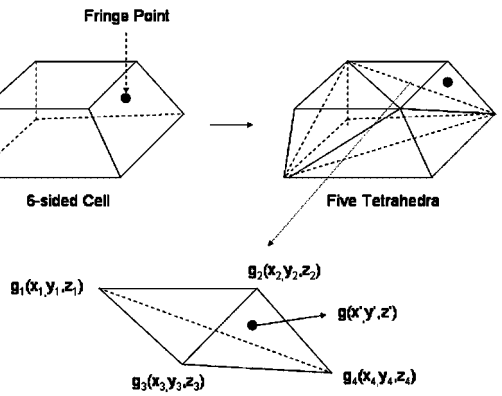

Figure A2. Four tetrahedra divided into a six-sided cell for interpolation.

where a_i $(i = 1, 2, 3, 4)$ are the coefficients, which are found by Cramer's rule using the four known variables, g_i, and the coordinates of its corresponding four vertices (x_i, y_i, z_i). A detailed explanation can be found in Reference [35].

APPENDIX B: FORCE AND TORQUE ON RBC DUE TO DEPLETION INTERACTION ENERGY

The depletion interaction model described in Reference [12] is used to account for RBC aggregation. According to the model, the total interaction energy per unit surface between two infinite plane surfaces representing RBC surfaces brought into close contact by the use of polymers such as dextran (DEX) or poly ethylene glycol (PEG) is the sum of the depletion attractive and electrostatic repulsive energies, with negligible van der Waals interactions

$$W_T = W_D + W_E \tag{B1}$$

DOI: 10.1002/fld

where W_D, W_E are the depletion interaction and electrostatic energies per unit surface, respectively. The depletion energy is in the form

$$W_D = -2\Pi\left(\Delta - \frac{d}{2} + \delta - P\right) \quad \text{when } \left(\frac{d}{2} - \delta + P\right) < \Delta \tag{B2}$$

$$W_D = 0 \quad \text{when } \left(\frac{d}{2} - \delta + P\right) > \Delta \tag{B3}$$

where Π, Δ, d, δ and P are the osmotic pressure term, depletion thickness, intercellular distance, RBC glycocalyx thickness (5 nm) and penetration depth, respectively. The osmotic pressure term, Π, and the depletion thickness, Δ, are functions of the molecular weight of the polymer and of the polymer concentration, C_p. The penetration depth, P, is a function of the polymer concentration, according to

$$P = \delta(1 - e^{-C_p/C_b}) \tag{B4}$$

where C_b is the penetration constant of the polymer in solution. The electrostatic energy is expressed in the form

$$W_E = \frac{\sigma^2}{\delta^2 \varepsilon \varepsilon_o k^3} \sinh(k\delta)(e^{k\delta - kd} - e^{-kd}) \quad \text{when } d \geqslant 2\delta \tag{B5}$$

$$W_E = \frac{\sigma^2}{\delta^2 \varepsilon \varepsilon_o k^3}(2k\delta - kd) - (e^{-k\delta} + 1)\sinh(k\delta - kd) - \sinh(k\delta)e^{-kd} \quad \text{when } d < 2\delta \tag{B6}$$

where σ, ε, ε_o, and k are the surface charge density of RBC, the relative permittivity of the solvent, the permittivity of the vacuum, and the Debye–Huckel length, respectively. The above formulation predicts an optimal polymer concentration for the interaction energy. The interaction energy increases, reaches a maximum and then decreases as the concentration increases. Furthermore, the interaction energy gradually increases to reach a maximum and then decreases to zero as the two surfaces approach. When the surfaces approach a distance equal to the sum of their glycocalyx thicknesses, they experience a strong repulsive force (Figure 10).

We now extend this formulation to surfaces of arbitrary shape using Derjaguin's integral approximation. Bhattacharjee *et al.* [26] have used Derjaguin' formula to express the intercellular interaction energy between two curved surfaces using the surface element integration:

$$U \approx \int_{S_1} (\mathbf{n}_1 \cdot \mathbf{k}_1)(\mathbf{n}_2 \cdot \mathbf{k}_2) W(h)\, dS_1 \tag{B7}$$

where $\mathbf{n}_1$ and $\mathbf{n}_2$ are the outward unit normal vectors of the surface elements of particles 1 and 2, respectively (Figure B1), and S_1 is the surface of particle 1. Here, h is the local distance between the two surface elements, $\mathbf{k}_1$ and $\mathbf{k}_2$ are the unit normal vectors of two parallel planes with the direction parallel to a line L, which connects the centres of two particles (Figure B1); thus $\mathbf{k}_1 = -\mathbf{k}_2$. Note that this theory assumes that an interaction occurs between two pairwise surface elements facing each other, and the particle with the smaller size of surface that faces the other particle is used for the integration domain. In the case of equal surfaces, either particle can be used for integration. Therefore, the surface of particle 1 is the integration domain in Equation (B7). Equation (B7) is used to obtain the interaction energy between two ellipsoidal RBCs in this study.

DOI: 10.1002/fld

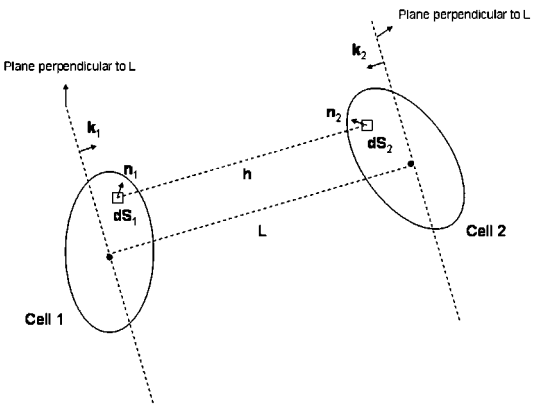

Figure B1. Surface elements of Cells 1 and 2.

The integration of Equation (B7) based on the surface element integration is over the entire surface of particle 1. However, we use only the surface of particle 1 that faces particle 2 for the integration, since only the volume elements between the RBC surfaces in close contact contribute to the interaction energy, based on the depletion interaction model. The vector forms of the surface elements $\mathrm{d}S_1$, $\mathrm{d}S_2$ of cells 1 and 2 are obtained by

$$\mathrm{d}\mathbf{S}_1 = \mathbf{n}_1\,\mathrm{d}S_1, \qquad \mathrm{d}\mathbf{S}_2 = \mathbf{n}_2\,\mathrm{d}S_2 \tag{B8}$$

respectively. In order to find two pairwise surface elements of cells 1 and 2, we identify the surface elements facing each other; for example, for cell 1, the elements facing each other are identified when the dot products of the surface elements of cell 1 and $\mathbf{k}_1$ are larger than zero. The conditions for identifying the surface elements of cells 1 and 2 facing each other are therefore

$$\mathrm{d}\mathbf{S}_1 \cdot \mathbf{k}_1 > 0, \qquad \mathrm{d}\mathbf{S}_2 \cdot \mathbf{k}_2 > 0 \tag{B9}$$

The term $(\mathbf{n}_1 \cdot \mathbf{k}_1)\,\mathrm{d}S_1$ of Equation (B7) is the projected surface element on the plane of $\mathbf{k}_1$. We define the projected surface element $\mathrm{d}Q_1$ and its vector $\mathrm{d}\mathbf{Q}_1$ of the surface element $\mathrm{d}\mathbf{S}_1$ identified by Equation (B9) on the plane of $\mathbf{k}_1$ as

$$\mathrm{d}Q_1 = \mathrm{d}\mathbf{S}_1 \cdot \mathbf{k}_1, \qquad \mathrm{d}\mathbf{Q}_1 = (\mathrm{d}\mathbf{S}_1 \cdot \mathbf{k}_1)\mathbf{k}_1 \tag{B10}$$

Likewise, for cell 2, we define

$$\mathrm{d}Q_2 = \mathrm{d}\mathbf{S}_2 \cdot \mathbf{k}_2, \qquad \mathrm{d}\mathbf{Q}_2 = (\mathrm{d}\mathbf{S}_2 \cdot \mathbf{k}_2)\mathbf{k}_2 \tag{B11}$$

The distance h and its vector $\mathbf{h}$, which is parallel to L in Figure B1, is the distance between a surface element $\mathrm{d}S_1$ of cell 1 and the corresponding pairwise surface element $\mathrm{d}S_2$ of cell 2. The total interaction energy in Equation (B7) can then be written as

$$U = \int_{S_1} (\mathbf{n}_1 \cdot \mathbf{k}_1)(\mathbf{n}_2 \cdot \mathbf{k}_2) W(h)\,\mathrm{d}S_1 = \int_{Q_1} (\mathbf{n}_2 \cdot \mathbf{k}_2) W(h)\,\mathrm{d}Q_1 \tag{B12}$$

where $\mathbf{n}_2$ is the direction vector of the pairwise surface element $\mathrm{d}\mathbf{S}_2$ corresponding to $\mathrm{d}\mathbf{S}_1$ of cell 1.

DOI: 10.1002/fld

The force corresponding to the interaction energy for cell 1 can be expressed as

$$\mathbf{F}_1^{\mathrm{A}} = -\frac{\partial U}{\partial \mathbf{h}} = -\int_{Q_1} (\mathbf{n}_2 \cdot \mathbf{k}_2) \frac{\partial W(h)}{\partial \mathbf{h}} \, \mathrm{d}Q_1 \tag{B13}$$

The torque generated by the interaction energy for cell 1 can now be found by

$$\mathbf{T}_1^{\mathrm{A}} = -\int_{Q_1} \mathbf{r}_{\mathrm{c}1} \times (\mathbf{n}_2 \cdot \mathbf{k}_2) \frac{\partial W(h)}{\partial \mathbf{h}} \, \mathrm{d}Q_1 \tag{B14}$$

where $\mathbf{r}_{\mathrm{c}_1}$ is the distance vector from the centre of cell 1 to $\mathrm{d}\mathbf{Q}_1$, and $\mathbf{T}^{\mathrm{A}}$ is the torque due to the attractive force on cell 1. The force and torque of cell 2 due to the interaction energy are then opposite in direction and the same in magnitude, so that

$$\mathbf{F}_2^{\mathrm{A}} = -\mathbf{F}_1^{\mathrm{A}} \tag{B15}$$

$$\mathbf{T}_2^{\mathrm{A}} = -\mathbf{T}_1^{\mathrm{A}} \tag{B16}$$

RBCs in plasma experience both fluid and interaction forces between the cells. Therefore the resultant force acting on cell i ($i = 1$ or 2) can be written in the form

$$\mathbf{F}_i = \mathbf{F}_i^{\mathrm{D}} + \mathbf{F}_i^{\mathrm{A}} \tag{B17}$$

where $\mathbf{F}_i^{\mathrm{D}}$ is the mechanical force due to the flow acting on cell i. Likewise, the resultant torque acting on cell i is the sum of the torques due to the flow and attractive force, such that

$$\mathbf{T}_i = \mathbf{T}_i^{\mathrm{D}} + \mathbf{T}_i^{\mathrm{A}} \tag{B18}$$

APPENDIX C: DISCRETIZATION AND SOLUTION METHOD

Equations (1)–(3) are solved by Chorin's pressure correction method [27]. The method divides the velocity field into vortical and irrotational components

$$\mathbf{v}^{n+1} = \mathbf{v}' + \mathbf{v}_o \tag{C1}$$

The vortical velocity, $\mathbf{v}'$, is due to the viscous effects, and the irrotational velocity, $\mathbf{v}_o$, is a result of temporal changes in the dynamic pressure α

$$p^{n+1} = p^n + \alpha \tag{C2}$$

Thus, Equation (2) is divided into two steps for solving the vortical velocity field with the old pressure field (Step I) and the irrotational velocity field (Step II), as

$$\int \rho \frac{\mathbf{v}' - \mathbf{v}^n}{\Delta t} \, \mathrm{d}V + \int \rho(\mathbf{v}' \cdot \nabla)\mathbf{v}' \, \mathrm{d}V = -\int p^n \mathbf{n} \, \mathrm{d}A + \int \boldsymbol{\tau}(\mathbf{v}') \cdot \mathbf{n} \, \mathrm{d}A \tag{C3}$$

$$\int \rho \frac{\mathbf{v}^{n+1} - \mathbf{v}'}{\Delta t} \, \mathrm{d}V = -\int \alpha \mathbf{n} \, \mathrm{d}A \tag{C4}$$

DOI: 10.1002/fld

where the superscript n denotes the values at $t=t^n$ and $n+1$, the values at $t=t^{n+1}$; $\Delta t=t^{n+1}-t^n$. These momentum equations coupled with continuity equation at t^{n+1}, yield

$$\int \nabla\phi\cdot\mathbf{n}\,\mathrm{d}A=\int \rho\mathbf{v}'\cdot\mathbf{n}\,\mathrm{d}A \tag{C5}$$

by expressing the irrotational velocity $\mathbf{v}_o$ in terms of the gradient of a potential

$$\mathbf{v}_o=-\frac{\nabla\phi}{\rho} \tag{C6}$$

The pressure correction term, α, is related to the velocity potential ϕ by

$$\alpha=\frac{\phi}{\Delta t} \tag{C7}$$

which can be obtained using Equations (C1) and (C4).

Discretization of the equations is performed based on the generalized coordinates (ξ,η,ζ). For instance, consider the convective term in the momentum equation, which has three components of x, y, z in the Cartesian coordinate system

$$\int \mathbf{v}\cdot\nabla v_i\,\mathrm{d}V=\int\left((\mathbf{v}\cdot\nabla\xi)\frac{\partial v_i}{\partial\xi}+(\mathbf{v}\cdot\nabla\eta)\frac{\partial v_i}{\partial\eta}+(\mathbf{v}\cdot\nabla\zeta)\frac{\partial v_i}{\partial\zeta}\right)\mathrm{d}V \tag{C8}$$

The three right-hand side terms of Equation (C8) based on (ξ,η,ζ) are obtained by the chain rule

$$\frac{\partial}{\partial x_i}=\frac{\partial}{\partial\xi}\frac{\partial\xi}{\partial x_i}+\frac{\partial}{\partial\eta}\frac{\partial\eta}{\partial x_i}+\frac{\partial}{\partial\zeta}\frac{\partial\zeta}{\partial x_i} \tag{C9}$$

where x_i is x, y, or z. For the volume integral as well as the surface integral based on finite volume formulation, the first-order derivative terms are discretized by a second-order central difference scheme. For example,

$$\frac{\partial v_i}{\partial\xi_i}=\frac{v_i^{i+1}-v_i^{i-1}}{2\Delta\xi_i} \tag{C10}$$

where ξ_i is ξ, η, or ζ. For the surface integral, at the surface with ξ direction, the first derivative terms are discretized as follows:

$$\frac{\partial v_i}{\partial\xi}=\frac{v_i^{i+1,j,k}-v_i^{i,j,k}}{\Delta\xi} \tag{C11}$$

$$\frac{\partial v_i}{\partial\eta}=\frac{1}{2}\left(\frac{v_i^{i,j+1,k}-v_i^{i,j-1,k}}{2\Delta\eta}+\frac{v_i^{i+1,j+1,k}-v_i^{i+1,j-1,k}}{2\Delta\eta}\right) \tag{C12}$$

$$\frac{\partial v_i}{\partial\zeta}=\frac{1}{2}\left(\frac{v_i^{i,j,k+1}-v_i^{i,j,k-1}}{2\Delta\zeta}+\frac{v_i^{i+1,j,k+1}-v_i^{i+1,j,k-1}}{2\Delta\zeta}\right) \tag{C13}$$

A detailed explanation of the discretization for the other types of control volumes can be found in Reference [35].

DOI: 10.1002/fld

The nonlinear discretized equations are then linearized by the Newton–Raphson method. The set of linearized algebraic equations is

$$\sum A_{\alpha\beta\gamma} v_{\alpha\beta\gamma} = d_{i,j,k} \tag{C14}$$

where

$$\alpha = i-1, i, i+1 \tag{C15}$$

$$\beta = j-1, j, j+1 \tag{C16}$$

$$\gamma = k-1, k, k+1 \tag{C17}$$

and $A_{\alpha\beta\gamma}$ are the coefficients of 27 terms and $d_{i,j,k}$ are functions of geometry and v_i at $t = t^n$. The unknown v_i in Equation (C14) are solved by a predictor corrector scheme [35].

ACKNOWLEDGEMENT

This work is supported by NIH Grant HL 52684.

REFERENCES

1. Popel AS, Johnson PC. Microcirculation and hemorheology. *Annual Review of Fluid Mechanics* 2005; **37**:43–69.
2. Lowe GDO. *Clinical Blood Rheology*. CRC Press: Boca Raton, FL, 1988.
3. Rampling MW *et al*. Influence of cell-specific factors on red blood cell aggregation. *Biorheology* 2004; **41**(2):91–112.
4. Linderkamp O *et al*. Red blood cell aggregation in preterm and term neonates and adults. *Pediatric Research* 1984; **18**(12):1356–1360.
5. Brooks DE, Goodwin JW, Seaman GVF. Interactions among erythrocytes under shear. *Journal of Applied Physiology* 1970; **28**(2):172–177.
6. Chien S. Shear dependence of effective cell volume as a determinant of blood viscosity. *Science* 1970; **168**(3934):977–979.
7. Bishop JJ *et al*. Rheological effects of red blood cell aggregation in the venous network: a review of recent studies. *Biorheology* 2001; **38**(2–3):263–274.
8. Reinke W, Gaehtgens P, Johnson PC. Blood viscosity in small tubes—effect of shear rate, aggregation, and sedimentation. *American Journal of Physiology* 1987; **253**(3):H540–H547.
9. Bishop JJ *et al*. Effects of erythrocyte aggregation and venous network geometry on red blood cell axial migration. *American Journal of Physiology—Heart and Circulatory Physiology* 2001; **281**(2):H939–H950.
10. Bishop JJ *et al*. Effect of erythrocyte aggregation on velocity profiles in venules. *American Journal of Physiology—Heart and Circulatory Physiology* 2001; **280**(1):H222–H236.
11. Chien S, Jan KM. Ultrastructural basis of mechanism of rouleaux formation. *Microvascular Research* 1973; **5**(2):155–166.
12. Neu B, Meiselman HJ. Depletion-mediated red blood cell aggregation in polymer solutions. *Biophysical Journal* 2002; **83**(5):2482–2490.
13. Evans A, Skalak R. *Mechanics and Thermodynamics of Biomembranes*. CRC Press: Boca Raton, FL, 1980.
14. Eggleton CD, Popel AS. Large deformation of red blood cell ghosts in a simple shear flow. *Physics of Fluids* 1998; **10**(8):1834–1845.
15. Pozrikidis C. Numerical simulation of the flow-induced deformation of red blood cells. *Annals of Biomedical Engineering* 2003; **31**(10):1194–1205.
16. Pozrikidis C. Effect of membrane bending stiffness on the deformation of capsules in simple shear flow. *Journal of Fluid Mechanics* 2001; **440**:269–291.
17. Bagchi P, Johnson PC, Popel AS. Computational fluid dynamic simulation of aggregation of deformable cells in a shear flow. *Journal of Biomechanical Engineering* 2005; **127**(6):1070–1080.

DOI: 10.1002/fld

18. Zhang L *et al*. Immersed finite element method. *Computer Methods in Applied Mechanics and Engineering* 2004; **193**(21–22):2051–2067.
19. Daux C *et al*. Arbitrary branched and intersecting cracks with the extended finite element method. *International Journal for Numerical Methods in Engineering* 2000; **48**(12):1741–1760.
20. Sun CH, Migliorini C, Munn LL. Red blood cells initiate leukocyte rolling in postcapillary expansions: a lattice Boltzmann analysis. *Biophysical Journal* 2003; **85**(1):208–222.
21. Sun CH, Munn LL. Particulate nature of blood determines macroscopic rheology: a 2-D lattice Boltzmann analysis. *Biophysical Journal* 2005; **88**(3):1635–1645.
22. Dougherty FC. *Development of a Chimera Grid Scheme with Applications to Unsteady Problems*. Stanford University, 1985.
23. Hu HH. Direct simulation of flows of solid-liquid mixtures. *International Journal of Multiphase Flow* 1996; **22**(2):335–352.
24. Nirschl H, Dwyer HA, Denk V. 3-Dimensional calculations of the simple shear-flow around a single-particle between two moving walls. *Journal of Fluid Mechanics* 1995; **283**:273–285.
25. Dasgupta A *et al*. Numerical simulation of flow past an array of moving spherical particles. *AIAA Journal* 1994; **3283**:1–23.
26. Bhattacharjee S, Elimelech M, Borkovecb M. DLVO interaction between colloidal particles: beyond Derjaguin's approximation. *CROATICA CHEMICA ACTA CCACAA* 1998; **71**(4):883–903.
27. Chorin AJ. Numerical solution of incompressible flow problems. *Journal of Computational Physics* 1967; **2**:12–26.
28. Happel J, Brenner H. *Mechanics of Fluids and Transport Processes*: *Low Reynolds Number Hydrodynamics*. Academic Press: Lancaster, 1986.
29. Wakiya S. Viscous flows past a spheroid. *Journal of the Physical Society of Japan* 1957; **12**(10):1130–1141.
30. Clift R, Grace JR, Weber ME. *Bubbles*, *Drops*, *and Particles*. Academic Press: New York, 1978.
31. Kim S *et al*. Aggregate formation of erythrocytes in postcapillary venules. *American Journal of Physiology—Heart and Circulatory Physiology* 2005; **288**(2):H584–H590.
32. Bishop JJ *et al*. Relationship between erythrocyte aggregate size and flow rate in skeletal muscle venules. *American Journal of Physiology—Heart and Circulatory Physiology* 2004; **286**(1):H113–H120.
33. Durussel JJ *et al*. Effects of red blood cell hyperaggregation on the rat microcirculation blood flow. *Acta Physiologica Scandinavica* 1998; **163**(1):25–32.
34. Mchedlishvili G, Gobejishvili L, Beritashvili N. Effect of intensified red blood cell aggregability on arterial pressure and mesenteric microcirculation. *Microvascular Research* 1993; **45**(3):233–242.
35. Shahcheraghi N. *Numerical Study of Three Dimensional Incompressible Flow and Heat Transfer over a Stationary and Moving and Rotating Sphere in a Pipe*, *in Mechanical Engineering*. University of California: Davis, 1996.

DOI: 10.1002/fld